Modelling the Evolution of an Iron-Rich Layer in a Double Diffusive Regime

Barbara Zemskova
University of North Carolina at Chapel Hill

September 22, 2013

1 Introduction

1.1 Problem Background

Thanks to the recent success of the astroseismology component of the Kepler mission, renewed attention has been given to the mechanism that causes time-varying luminosity, or pulsations, in β-Cepheid stars. The pulsation mechanism for regular Cepheids is well-understood in terms of the kappa-mechanism. The pulsations are dependent on the opacity κ of the ionized layers of a star. This opacity is controlled by radiative processes, namely the absorption and re-emission of photons as they move away from the stellar core. However, the electrons in an ionized layer block photons and prevent radiative heat transport through the layer. From Kramer's Law, the opacity of an outer layer is found by: $\kappa = \rho/T^{3.5}$, where ρ is the density in the layer and T is the temperature. If the outward pressure beneath the layer decreases, then the layer contracts inwards, and its volume decreases. The energy that is released upon contraction of the layer partially ionizes the helium atoms, rather than increases the temperature of the layer, thus increasing the opacity. Heat is then transported through the layer less efficiently, so pressure builds up beneath the layer. This pressure is eventually enough to push the layer outward, thus increasing its volume. As the layer expands, the electrons recombine with the ions, and the density within the layer drops, such that the opacity consequently decreases, allowing greater heat transport through the layer. Eventually the pressure beneath the layer drops again, and the cycle repeats, resulting in periodic variations in the star's luminosity [3, 9].

However, the role of helium partial ionization zones, as presented in the standard kappa mechanism, is sensitively dependent on the temperature of the star. For a hot star with effective temperature greater than 7500 K, the partial ionization zones are located too close to the star's outer surface, and they are unable to drive significant pulsations. For cooler stars with effective temperature less than 5500 K, the partial ionization zones are too close to stellar core, and heat can be transported by convection rather than by radiation, and does not build up beneath the partial ionization zones. The regular Cepheids, which are located on the instability strip, are within the perfect temperature range to exhibit these pulsations described by the kappa mechanism. The β-Cepheids, on the other hand, have too high temperatures to have helium partial ionization zones, so one would not expect them

to pulsate. However, these stars do exhibit pulsations. It has been recently thought that they may have iron partial ionization zones that could explain their periodic pulsations in a similar way [4]. These stars are larger and brighter than regular Cepheids, so it is important to understand the mechanism that drives their pulsations for other astrophysical applications as well.

If such iron partial ionization layers could be responsible for pulsations in β-Cepheids, how can these layers form and is there evidence that such iron layers exist in stars? To see how iron layers may form, note that there are two opposing forces that act on atoms: radiative levitation and gravitational settling. The radiative levitation acts away from the stellar core due to the upward momentum on atoms exerted by photons that are emitted from the core, while the gravitational settling acts toward the stellar core. The total settling velocity, V, of an atom can be expressed as:

$$V = (g_{rad} - g)\frac{mD}{kT} \tag{1}$$

where g_{rad} is radiative acceleration (away from the core), g is the gravitational acceleration (toward the core), m is the element mass, D is the molecular diffusion coefficient, k is the Boltzman constant, and T is the stellar temperature [8]. The force balance is element-dependent, not only because of the element mass, but also because the radiative acceleration depends on the chemical species in question. Therefore, the sign of the total settling velocity, which is determined by the sign of $g_{rad} - g$, is element-dependent. This dependency is illustrated in the work of [7], where profiles for selected chemical species are shown (see Figure (1)). For each element, Figure (1) shows $\log(g_{rad}/g)$ as a function of the distance away from the stellar core, such that -6 on the x-axis indicates outer layers, and 0 indicates proximity to the stellar core. For certain elements, such as Mg, $\log(g_{rad}/g) < 0$ in all regions, so the radiative levitation is less than the gravitational settling, and the total settling velocity is always toward the core. For other elements, such as Mn, Ca, and Fe, there are regions where the radiative levitation exceeds the gravitational settling. The case of iron is particularly interesting because there is a region where $\log(g_{rad}/g) > 0$, with regions where $\log(g_{rad}/g) < 0$ both above and below it. As a result, there is a zone where the iron atoms converge in a "pinched layer", as shown in Figure (2). It is due to this mechanism that iron layers could exist near a stellar photosphere.

In this study, we attempt to describe several characteristics of iron "pinched layer", such as the thickness of the layer, iron profile, and maximum iron concentration. Additionally, we show that depending on the system parameters and the mass of iron, the layer may be either double diffusively or fully convectively unstable, which would alter the iron concentration profile. Note that the analysis in this project is not specific to iron atoms, and the results can be generalized to any system that fits the formulation described above.

1.2 Governing Equations

Here, we consider a domain that is thin compared with the local system scaleheight and assume that both the background temperature and adiabatic temperature gradients are constant within that region. In astrophysical systems, the background temperature decreases away from the stellar core toward the outer layers, thus the background temperature gradient is negative. However, because the fluid is not incompressible, the adiabatic temperature

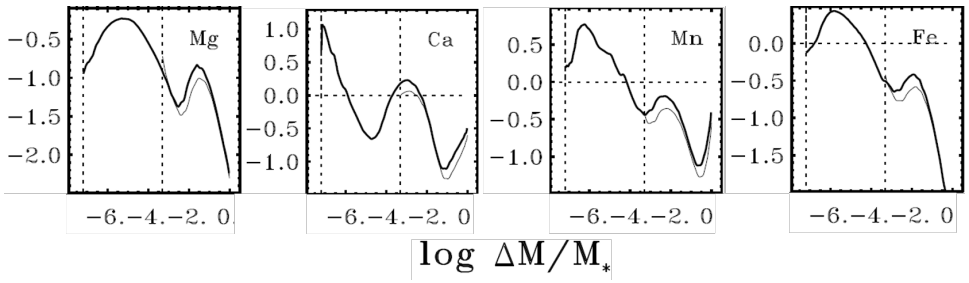

Figure 1: Profiles of radiative acceleration of selected elements normalized with respect to local gravity as a function of distance from the stellar core for a main sequence star. For certain elements like Mg, gravitational settling exceeds the radiative levitation. For some other elements, there are layers where radiative levitation exceeds gravitational settling [7]).

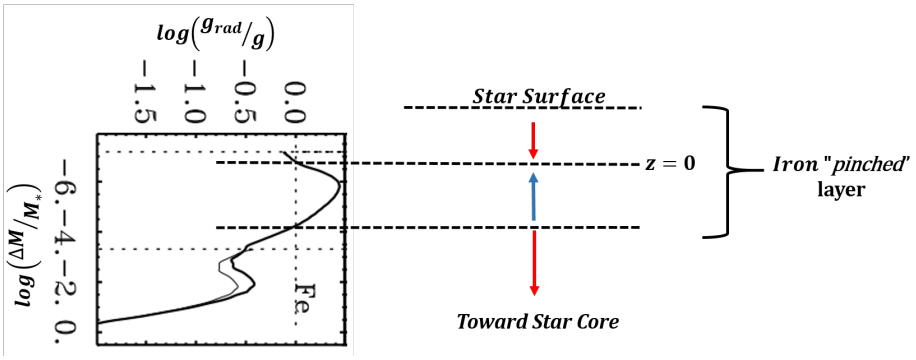

Figure 2: Model of a system with an iron converging zone based on a profile from Figure (1). In this "pinched" layer, total settling velocity is positive (radiative levitation exceeds gravitational settling) for $z < 0$, and total settling velocity is negative (gravitational settling exceeds radiative levitation) for $z > 0$.

gradient is nonzero. Since the difference between background and adiabatic temperature gradients is positive, the combined effect of the temperature gradients makes the fluid stably stratified . The governing equations for the system are ([5]):

$$\frac{\partial \vec{u}}{\partial t} + \vec{u} \cdot \nabla \vec{u} = -(1/\rho_0)(\nabla p - \rho \vec{g}) + \nu \nabla^2 \vec{u}, \tag{2}$$

$$\frac{\partial T}{\partial t} + \vec{u} \cdot \nabla T + w \left(\frac{\partial \bar{T}_{back}}{\partial z} - \frac{\partial \bar{T}_{adiab}}{\partial z} \right) = \kappa_T \nabla^2 T, \tag{3}$$

$$\frac{\partial C}{\partial t} + \vec{u} \cdot \nabla C + \frac{\partial}{\partial z}(V_s C) = \kappa_C \nabla^2 C, \tag{4}$$

$$\nabla \cdot \vec{u} = 0 \tag{5}$$

where $\vec{u} = (u, v, w)$ is the velocity field, T is the temperature, C is the iron concentration, p is the pressure, κ_T is the thermal diffusivity, κ_C is the diffusivity of the iron atoms, ν is the molecular viscosity, $\bar{T}_{back}$ is the background temperature and $\bar{T}_{adiab}$ is the adiabatic temperature. The only change to the original advection-diffusion equations is the added "settling" velocity term V_s for the iron, which depends on the vertical position z. These equations are then non-dimensionalized with the following length and time scales, as described in [6]:

$$d = [l] = \left(\frac{\kappa_T \nu}{g \alpha \bar{T}_z} \right)^{1/4}, \tag{6}$$

$$[t] = \frac{d^2}{\kappa_T}, \tag{7}$$

$$[u] = \frac{\kappa_T}{d}, \tag{8}$$

$$[T] = \bar{T}_z d, \tag{9}$$

$$[C] = \frac{\alpha \bar{T}_z d}{\beta}. \tag{10}$$

where we have defined for simplicity $\bar{T}_z = \frac{\partial \bar{T}_{back}}{\partial z} - \frac{\partial \bar{T}_{adiab}}{\partial z}$, α is the thermal expansion coefficient, and β is the compositional contraction coefficient. In this non-dimensionalization, the length scale d corresponds to the typical horizontal length scale of a finger, and the time scale is the thermal diffusion time scale. From non-dimensionalization, the governing equations can be re-written as follows with 2 non-dimensional parameters:

$$\frac{1}{\mathrm{Pr}}\left(\frac{\partial \vec{u}}{\partial t} + \vec{u} \cdot \nabla \vec{u}\right) = -\nabla p + (T - S)\hat{k} + \nabla^2 \vec{u}, \tag{11}$$

$$\frac{\partial T}{\partial t} + \vec{u} \cdot \nabla \vec{T} + w = \nabla^2 T, \tag{12}$$

$$\frac{\partial C}{\partial t} + \vec{u} \cdot \nabla \vec{C} + \frac{\partial}{\partial z}(V_s C) = \tau \nabla^2 C, \tag{13}$$

$$\nabla \cdot \vec{u} = 0 \tag{14}$$

where Pr is the Prandtl number, defined as $\mathrm{Pr} = \nu/\kappa_\mathrm{T}$, and $\tau = \kappa_C/\kappa_T$ is the ratio of the diffusion coefficients. Here, $V_s(z)$ is the non-dimensionalized settling velocity. For double diffusive convection to occur, it is important that $\tau \ll 1$. When a warm fluid parcel with

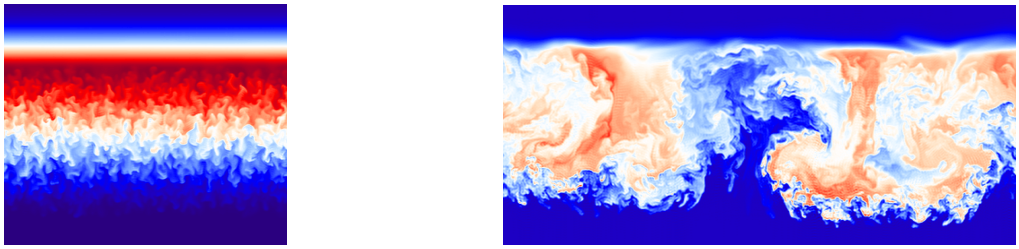

Figure 3: An example of fingering convection, a type of double diffusive instability (left) for a system with $\tau = \text{Pr} = 0.1$, $s = 0.001$, $C_0 = 466$, and an example of full convection (right) with $\tau = \text{Pr} = 0.1$, $s = 0.01$, $C_0 = 4500$. Warm colors show fluid parcels with higher iron concentration, cooler colors with lower concentration. Fingers with higher iron concentration extend downward, and the ones with lower iron concentration extend upward.

high compositional concentration is moved downward into cooler ambient fliud, it naturally rises because it is more buoyant. However, if the thermal diffusion time scale is less than the amount of time it takes the parcel to move back to its original position, then the fluid parcel loses its heat, but retains its concentration. As a result, it becomes heavier than the ambient and sinks, forming a downward finger. Equally, a cool parcel with low composition concentration would form an upward extending finger when perturbed into a warm layer. The result of such double diffusive instability is fingering convection, an example of which is shown in Figure (3). An example of a fully-convective system is shown to the right for comparison.

2 Evolution of the Background Profiles

We begin our investigation by considering the evolution of the iron concentration, assuming there is no fluid motion. Thus, we seek solution to a one-dimensional advection-diffusion equation with respect to the iron concentration C:

$$\frac{\partial C}{\partial t} + \frac{\partial}{\partial z}(V_s C) = \tau \frac{\partial^2 C}{\partial z^2}. \tag{15}$$

Here $V_s(z)$ is the iron settling/levitation velocity, defined as $V_s = -sz$ where s is a constant. Indeed, from the schematic of the iron "pinched layer" in Figure (2), we see that we can approximate $V_s(z)$ near the center of this layer ($z = 0$) with a linear function. We model $V_s(z)$ such that the downward gravitational settling dominates in the upper half of the domain ($z > 0$), and the upward radiative levitation dominates in the lower half of the domain ($z < 0$). Therefore we choose $V_s = -sz$ with $s > 0$.
An analytical solution to this equation is a Gaussian in the form:

$$C(z,t) = \frac{C_0}{\sqrt{2\pi f(t)}} e^{-\frac{z^2}{2f(t)}}, \tag{16}$$

where $\sqrt{f(t)}$ is the width of the Gaussian at time t. C_0 is a non-dimensional term that is related to total column density of iron, such that $C_{dim} = C_0[C]$ and $\int C_{dim} dz$ is the column

density of iron in the layer,Σ_0. This implies that $C_0 = \frac{\alpha \bar{T}_z}{\beta \Sigma_0} d$.
Plugging in (16) into (15), we can solve for $f(t)$:

$$f = \frac{\tau + \tilde{b} e^{-2st}}{s}, \tag{17}$$

where $\tilde{b}$ is some initial width of the Gaussian at time t_0. Note that $f(t) \to \tau/s = f_\infty$ as $t \to \infty$. Therefore, in absence of instabilities the ultimate laminar steady state concentration profile is in the form:

$$C(z) = \frac{C_0}{\sqrt{2\pi f_\infty}} e^{-\frac{z^2}{2f_\infty}}. \tag{18}$$

3 Stability of Double Diffusive Convection with Particle Settling

As the width of the Gaussian decreases and the iron concentration in the "pinched layer" increases, the concentration profile becomes steeper and steeper at a certain place in the layer, and the system may eventually become double diffusively unstable. In order to study the stability of the iron layer to double diffusive convection one must analyze the problem allowing a spatially-varying background that also evolves in time. However, as such formulation is not trivial, we begin by approaching the problem in a simpler way.

3.1 Stability of a system with linear gradients

The Gaussian concentration profile from (16) has maximum gradient at the inflection points that occur at $z = \pm\sqrt{f}$. Further, it is most unstable where the maximum concentration gradient is positive, at $z = -\sqrt{f}$. In this approach, we perform a local stability analysis near this most unstable point $z = -\sqrt{f}$ to determine whether the system becomes double diffusively unstable or not. Near this point, the background temperature and concentration profiles can be approximated by linear functions with constant gradients $\bar{T}_z = \frac{\partial \bar{T}_{back}}{\partial z} - \frac{\partial \bar{T}_{adiab}}{\partial z}$ and $\frac{\partial \bar{C}_{back}}{\partial z}$. We also assume that the time scale for the development of the instabilities is much less than the time scale for the evolution of the background. We can then apply the "frozen-in" approximation, which assumes that the background temperature and concentration gradients are constant not only in space, but also in time. These simplifications recover the approach from [1], but the equations contain an additional settling term in the iron concentration equation. We then apply the linear stability theory by linearizing the

governing equations, such that:

$$\frac{1}{\mathrm{Pr}}\frac{\partial u}{\partial t} = -\frac{\partial p}{\partial x} + \nabla^2 u, \tag{19}$$

$$\frac{1}{\mathrm{Pr}}\frac{\partial v}{\partial t} = -\frac{\partial p}{\partial y} + \nabla^2 v, \tag{20}$$

$$\frac{1}{\mathrm{Pr}}\frac{\partial w}{\partial t} = -\frac{\partial p}{\partial z} + (T - C) + \nabla^2 w, \tag{21}$$

$$\frac{\partial T}{\partial t} + w = \nabla^2 T, \tag{22}$$

$$\frac{\partial C}{\partial t} + \frac{w}{R_0} + V\frac{\partial C}{\partial z} = \tau\nabla^2 C, \tag{23}$$

$$\frac{\partial u}{\partial x} + \frac{\partial v}{\partial y} + \frac{\partial w}{\partial z} = 0. \tag{24}$$

Here, we have defined another nondimensional parameter, $R_0 = 1/(\partial\bar{C}/\partial z)$, where $\partial\bar{C}/\partial z$ is the non-dimensional gradient of iron concentration at $z = -\sqrt{f}$. In the dimensional sense, R_0 is the ratio of the stabilizing temperature gradient to the destabilizing compositional gradient, such that ${R_0}^{dim} = (\alpha {\bar{T}_z}^{dim})/(\beta {\bar{C}_z}^{dim})$. At the point where the Gaussian is most unstable ($z = -\sqrt{f}$), $\bar{C}_z$ is maximum and R_0 is minimum, so we have:

$$\bar{C}_z = \frac{C_0}{f\sqrt{2\pi e}}, \tag{25}$$

and

$$R_0 = \frac{f\sqrt{2\pi e}}{C_0}. \tag{26}$$

Note how in the linearized equation for particle concentration, we have also assumed that the settling velocity is locally constant at value V. Expressing the quantities u, w, p, T, C in the form $Q = \hat{Q}e^{ilx+ikz+\lambda t}$, where $\hat{Q}$ represents the mean quantity, we obtained a cubic for the growth rate λ, which is similar to the original cubic of [1], but has additional imaginary terms in the coefficients that are associated with the particle settling.

$$\lambda^3 + a_2\lambda^2 + a_1\lambda + a_0 = 0, \text{ where} \tag{27}$$

$$a_2 = ikV + K^2(\tau + 1 + \mathrm{Pr}) \tag{28}$$

$$a_1 = K^2(ikV)(\mathrm{Pr} + 1) + \mathrm{K}^4(\tau\mathrm{Pr} + \tau + \mathrm{Pr}) + \frac{\mathrm{Pr}(\mathrm{m}^2 + \mathrm{l}^2)}{\mathrm{K}^2}(1 - \frac{1}{\mathrm{R}_0}) \tag{29}$$

$$a_0 = \frac{\mathrm{Pr}}{K^2}(ikV)(K^6 + (m^2 + l^2)) + K^6\mathrm{Pr}\tau + \frac{\mathrm{Pr}(\mathrm{m}^2 + \mathrm{l}^2)}{\mathrm{K}^2}(\tau - \frac{1}{\mathrm{R}_0}) \tag{30}$$

$$\tag{31}$$

where $K^2 = l^2 + m^2 + k^2$. However, after examining the solutions to the cubic for different l and k values, we find that the fastest growing mode is still $k = 0$, as in the case without settling. This means that the added settling term, ikV, does not impact the initial development of the instabilities.

Given the nondimensional parameters Pr, τ, and R_0 of the system, one can determine the maximum growth rate of the instability λ_{max} and its associated horizontal wave number l_{max}. We then take $k = 0$ and maximize λ with respect to l, resulting in a quadratic:

$$b_2\lambda^2 + b_1\lambda + b_0 = 0, \text{ where} \tag{32}$$

$$b_2 = 1 + \mathrm{Pr} + \tau \tag{33}$$

$$b_1 = 2l^2(\tau + \mathrm{Pr} + \tau\mathrm{Pr}) \tag{34}$$

$$b_0 = 3\tau\mathrm{Prl}^4 + \mathrm{Pr}(\tau - \frac{1}{\mathrm{R_0}}); \tag{35}$$

λ_{max} and and l_{max} can be found by solving (27) and (32) simultaneously, using a Newton method for instance.

3.2 Estimation of width of the Gaussian at the onset of instability

[1] showed that the stability of the system depends on R_0. A system is double diffusively unstable when $1 < R_0 < 1/\tau$. If $R_0 > 1/\tau$, then the system is stable, and as R_0 becomes less than 1, the system becomes fully convective. We can therefore use these criteria to determine whether an iron layer is stable, double diffusively unstable, or fully convective. In the early stages of the evolution the iron layer is mostly likely stable, but as the Gaussian concentration profile contracts with time, $\bar{C}_z$ increases and R_0 decreases at the point of maximum instability, $z = -\sqrt{f}$. We can then estimate the width of the Gaussian profile when a system first becomes marginally unstable to double diffusion. This happens when $R_0 = 1/\tau$, which from (26) corresponds to:

$$f(t^*) = f_{crit} = \frac{C_0}{\tau\sqrt{2\pi e}}. \tag{36}$$

We see that whether an iron layer, with given input parameters τ, Pr, and s, ever becomes unstable and at which width the instabilities occur, depends on the total surface density of the system. Figure (4) shows $\sqrt{f_{crit}/f_\infty}$ as a function of C_0. If $f_{crit} < f_\infty$, the evolving concentration profile would reach a steady state laminar solution before attaining the width at which double diffusive instabilities appear. However, if $f_{crit} > f_\infty$, then double diffusive instabilities appear when the concentration profile reaches the width $\sqrt{f_{crit}}$. We define C_{crit} as the input mass for which $f_{crit} = f_\infty$: $C_{crit} = \frac{\tau^2\sqrt{2\pi e}}{s}$. For systems with $C_0 < C_{crit}$, double diffusive instabilities are not predicted to occur, and the concentration profile should relax to a laminar solution. Conversely, for systems with $C_0 > C_{crit}$, the system is predicted to be double diffusively unstable. The subsequent evolution of the concentration profiles for such systems are analyzed in the next section.

4 Simplified model for the long-term evolution of the system

In order to study the evolution of layers that become double diffusively unstable, we need to consider the turbulent transport of iron in addition to diffusion and to the settling/levitation

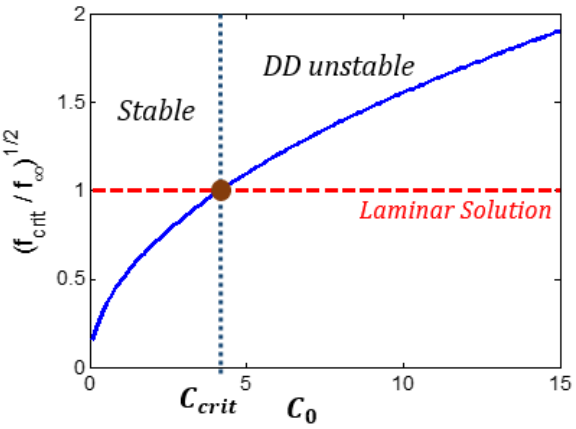

Figure 4: Diagram of stable regions and double diffusively unstable regions with respect to input mass C_0. The system is stable if $f_{crit}/f_\infty \leq 1$. Therefore, if $C_0 < C_{crit}$ and the initial concentration profile has width greater than $\sqrt{f_\infty}$, the steady state concentration profile will converge to a laminar Gaussian solution of (18) and the system is stable. However, if $C_0 < C_{crit}$, double diffusive instabilities will develop before the system converges to a laminar solution.

balance. The 1D advection-diffusion equation used contains an additional term to model this effect:

$$\frac{\partial C}{\partial t} + \frac{\partial F_s}{\partial z} + \frac{\partial}{\partial z}(V_s C) = \tau \frac{\partial^2 C}{\partial z^2}, \tag{37}$$

where F_s is the turbulent flux, which can be defined in terms of a Nusselt number, Nu as:

$$F_s = -\tau \frac{\partial C}{\partial z}(\mathrm{Nu} - 1). \tag{38}$$

Therefore, (37) can be re-written as:

$$\frac{\partial C}{\partial t} + \frac{\partial}{\partial z}(V_s C) = \tau \frac{\partial}{\partial z}\left(\frac{\partial C}{\partial z}\mathrm{Nu}\right). \tag{39}$$

[2] proposed a new turbulent transport parametrization for double diffusive convection, which takes the form:

$$\mathrm{Nu} = 1 + \hat{\mathrm{C}}^2 \frac{\lambda^2}{\tau \mathrm{l}^2(\lambda + \tau \mathrm{l}^2)} \tag{40}$$

where $\hat{C} = 7$ is an empirical constant, and where λ and l, the growth rate and the wavenumber of the fastest growing mode respectively, are found from the linear stability analysis described in Section 3.1. Note that if the layer is stable and $\lambda = 0$, Nu $= 1$, so Equation (39) recovers the original advection-diffusion equation (15).
At steady state, we must solve:

$$V_s C = -szC = \tau \mathrm{Nu} \frac{\partial \mathrm{C}}{\partial \mathrm{z}}. \tag{41}$$

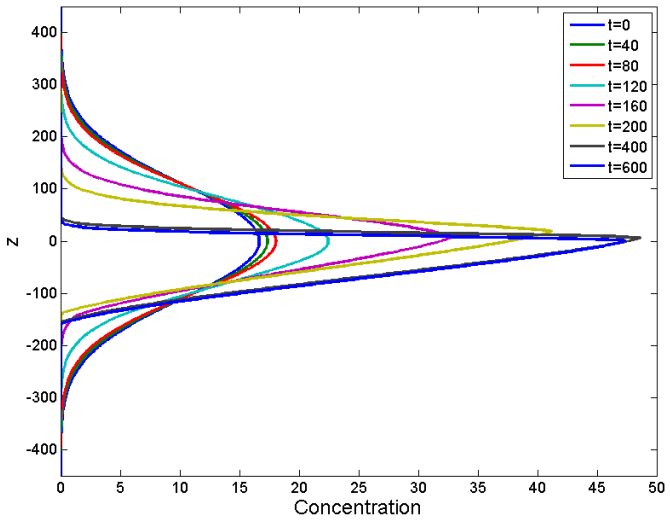

Figure 5: Time evolution of the iron concentration from numerical solution with the following parameters: $\tau = \mathrm{Pr} = 0.1$, $s = 0.001$, and $C_0 = 466$. The concentration profile is initially stable, but becomes double diffusively unstable after contraction, and is no longer of Gaussian form.

We wish to find an analytical expression for this steady-state solution. The difficulty arises because Nu is a function of λ and l, which depend on $R_0 = 1/C_z$, so Nu is a function of $\bar{C}_z$ as well.

We first solve (39) numerically to observe the time evolution of the iron concentration. Figure (5) shows the iron concentration profiles in the layer at different time steps. The concentration profile initially takes a stable Gaussian form, but eventually contracts enough to become double diffusively unstable. Once this happens, Nu becomes larger than 1 and turbulent fluxes become significant. After a while, we observe that the concentration converges to a steady-state, but it is no longer Gaussian. Figure(6) shows $\frac{\partial C}{\partial z}$ as a function of z in this steady-state solution. The profile has 3 parts: above z_1 and below z_2, $C_z < \tau$, so the system is stable to double diffusion and $\mathrm{Nu} = 1$. Between z_1 and z_2, $\tau < C_z < 1$, so the layer is double diffusively unstable. Since at z_1 and z_2 the instabilities are just triggered, $\lambda = 0$ and $\mathrm{Nu} = 1$, the steady-state at those two points implies (see Equation (41)):

$$-sz_1 C(z_1) = \tau C_z(z_1) = \tau^2, \tag{42}$$

$$-sz_2 C(z_2) = \tau C_z(z_2) = \tau^2. \tag{43}$$

Here we find that $C(z_1) = -f_\infty \tau / z_1$ and $C(z_2) = -f_\infty \tau / z_2$. For $z > z_1$ and for $z < z_2$, the system is stable and the concentration profile is Gaussian. Therefore, these parts of the

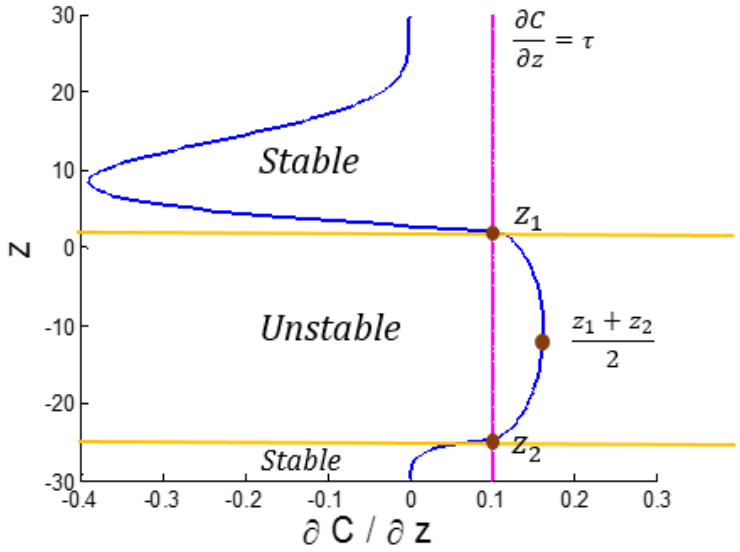

Figure 6: Schematic of the theoretical approach to a steady state concentration profile. The plot shows the derivative of steady state concentration profile from 1D simulation, $\frac{\partial C}{\partial z}$. The parts where $\frac{\partial C}{\partial z} < \tau$ are stable, while the parts where $\frac{\partial C}{\partial z} > \tau$ are double diffusively unstable. The two points, z_1 and z_2 are located where $\frac{\partial C}{\partial z} = \tau$.

concentration profile are expressed as:

$$C(z \geq z_1) = \frac{C_u}{\sqrt{2\pi f_\infty}} e^{-\frac{z^2}{2f_\infty}}, \tag{44}$$

$$C(z \leq z_2) = \frac{C_L}{\sqrt{2\pi f_\infty}} e^{-\frac{z^2}{2f_\infty}}. \tag{45}$$

where C_u and C_L are two constants to be determined. Using the expressions for $C(z_1)$ and $C(z_2)$, C_u and C_L can be expressed as:

$$C_u = -\sqrt{2\pi f_\infty} e^{\frac{{z_1}^2}{2f_\infty}} \frac{f_\infty \tau}{z_1}, \tag{46}$$

$$C_L = -\sqrt{2\pi f_\infty} e^{\frac{{z_2}^2}{2f_\infty}} \frac{f_\infty \tau}{z_2}. \tag{47}$$

In the region where $z_2 < z < z_1$, $C_z > \tau$. We approximate C_z using a parabola: $C_z = \tau + k(z_1 - z)(z - z_2)$ for some value k. The concentration profile in this region is then approximately:

$$C(z_2 < z < z_1) = C(z_2) + \int_{z_2}^{z} (\tau + k(z_1 - z)(z - z_2))\, dz =$$
$$C(z_2) + \tau(z - z_2) + \frac{k}{2}(z_1 - z_2)(z - z_2)^2 - \frac{k}{3}(z - z_2)^3. \tag{48}$$

Plugging in z_1 for z and the fact that $C(z_1) = -f_\infty \tau / z_1$, we obtain an equation relating k, z_1, and z_2.

Finally, we assume that at $\hat{z} = (z_1 + z_2)/2$ there is a balance between the advective flux $V_s C$ and turbulent flux F_s, such that:

$$-s\hat{z}C(\hat{z}) = \tau \mathrm{Nu}(\mathrm{C_z}(\hat{z}))\mathrm{C_z}(\hat{z}). \tag{49}$$

As a result of these assumptions, we obtain 3 equations for 3 unknowns: k, z_1, and z_2. Equation (50) is obtained from mass conservation by integrating the piecewise concentration profile. Equation (51)is found from plugging in z_1 for z in the cubic equation for $C(z_2 < z < z_1)$. Equation (52) incorporates the advective and turbulent fluxes at $\hat{z}$.

$$C_0 + \frac{\tau f_\infty}{z_1} e^{\frac{{z_1}^2}{2f_\infty}} \sqrt{\frac{\pi f_\infty}{2}} \left[1 - \mathrm{erf}\left(\frac{\mathrm{z_1}}{\sqrt{2\mathrm{f_\infty}}}\right)\right] + \frac{\tau f_\infty}{z_2} e^{\frac{{z_2}^2}{2f_\infty}} \sqrt{\frac{\pi f_\infty}{2}} \left[1 + \mathrm{erf}\left(\frac{\mathrm{z_2}}{\sqrt{2\mathrm{f_\infty}}}\right)\right] = 0 \tag{50}$$

$$f_\infty \tau - z_1 z_2 \left[\tau + \frac{k}{6}(z_1 - z_2)^2\right] = 0 \tag{51}$$

$$\frac{(\tau z_1 + z_2)^2}{4 z_1 z_2} - \mathrm{Nu}(\mathrm{C_z}(\hat{\mathrm{z}})) \left[\tau + \frac{\mathrm{k}(\mathrm{z_1} - \mathrm{z_2})^2}{4}\right] = 0 \tag{52}$$

These 3 equations can be solved for k, z_1, and z_2 using Newton's method for a given set of input parameters: τ, Pr, s, and C_0. Once these are known, piecewise steady state concentration profile $C(z)$ is:

$$C(z > z_1) = -\frac{f_\infty \tau}{z_1} e^{-\frac{z^2 - {z_1}^2}{2f_\infty}}, \tag{53}$$

$$C(z_2 \geq z \leq z_1) = -\frac{f_\infty \tau}{z_2} + \tau(z - z_2) + \frac{k}{2}(z_1 - z_2)(z - z_2)^2 - \frac{k}{3}(z - z_2)^3, \tag{54}$$

$$C(z < z_2) = -\frac{f_\infty \tau}{z_2} e^{-\frac{z^2 - {z_2}^2}{2f_\infty}}. \tag{55}$$

For example using $\tau = \mathrm{Pr} = 0.1$, $s = 0.01$, $f_\infty = 10$, Figure (7) shows the solutions for z_1, z_2, and k as functions of C_0. The value for z_1 approaches zero as C_0 increases, while z_2 decreases nonlinearly. The value of k decreases sharply and approaches a constant. These patterns are true for any choice of different input parameters of τ, Pr and s.

Furthermore, in Section 3.1 we defined $R_0 = 1/C_z$ and stated that double diffusive instabilites occur for $1 < R_0 < 1/\tau$. For $R_0 < 1$, the system is predicted to become fully-convective. In the unstable region $z_2 < z < z_1$, we approximated C_z as a parabola, which has a maximum at $\hat{z} = (z_1 + z_2)/2$, such that $C_{zmax} = \tau + (k/4)(z_1 - z_2)^2$. From $R_{0min} = 1/C_{zmax}$, for a given set of τ, Pr, s, we can find C_{conv}, the value of C_0 above which the layer is predicted to become fully convective. Figure (8) shows an example for a system with $\tau = \mathrm{Pr} = 0.1$, $s = 0.01$, $f_\infty = 10$. For this example, the theory predicts that the system will be fully convective if $C_0 > C_{conv} = 4600$.

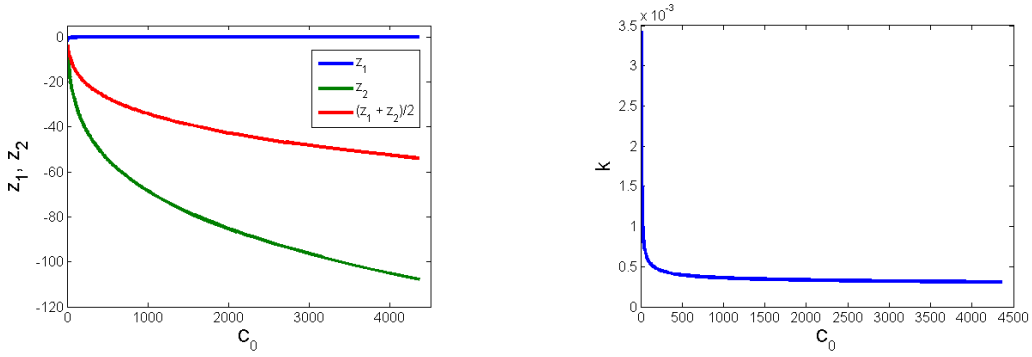

Figure 7: Plot on the left shows z_1 and z_2 as functions of input mass C_0; z_1 approaches zero, z_2 decreases nonlinearly as C_0 increases. Plot of the right shows k as a function of C_0; k rapidly decreases and approaches a constant as C_0 increases. Both of the plots are examples for a system with input parameters: $\tau = Pr = 0.1$, $s = 0.01$, $f_\infty = 10$.

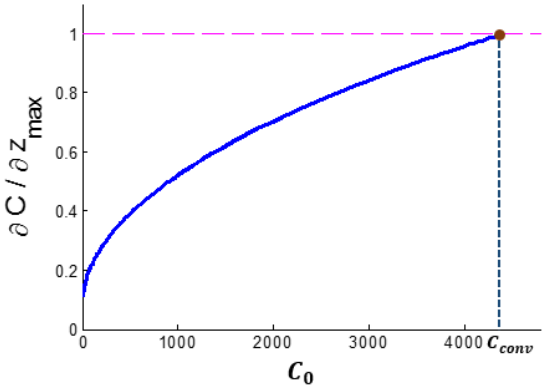

Figure 8: A plot of maximum $\frac{\partial C}{\partial z}$ as a function of C_0 for a system with $\tau = Pr = 0.1$, $s = 0.01$, $f_\infty = 10$. The piecewise steady state theory predicts C_{conv}, the input mass enough to make the system fully convective for which maximum $\frac{\partial C}{\partial z} = 1$.

5 Results of Numerical Simulations

In order to evaluate the theoretical predictions for the onset of the double diffusive instabilities, the steady state concentration profiles, and the surface densities above which double diffusive instabilites or full convection may occur, we have ran several 3-D numerical simulations.

5.1 Set-up of the 3D code

Our code solves equations (11) - (14) in a triply-periodic domain. The temperature perturbations are initialized with random noise. The initial concentration profile is a Gaussian of a form:

$$C_{init}(z) = \frac{C_0}{2\pi f_{init}} \tag{56}$$

where $f_{init} > f_{crit}$, chosen such that the iron layer is initially stable. This way we can determine whether the concentration profile will converge to a laminar solution, or whether double diffusive instabilites or full convection develop. To save computational time, f_{init} was typically taken to be $1.1 - 2f_{crit}$, where f_{crit} is given in Equation (36).

The typical width of a double diffusive finger being $7 - 10d$, the width of the domain (x-direction) was chosen as $100d$ to allow at least 10 fingers to develop in the system. From preliminary computations in a 2-dimensional domain, we have also that found artificial shear develop in the solutions. Therefore, we ran 3D simulations in a domain with a depth of $15d$ which is thick enough to allow the fluid motions to be 3-dimensional (to avoid this problem), but also thin enough to decrease the computational cost of the simulations.

The height of the domain (z direction) depended on the input parameters of the simulation. For most of the simulations, the vertical velocity was prescribed as a sine function of the form $V(z) = -K\sin((2\pi z)/\Gamma_z)$, where Γ_z is the height of the domain and $K = (s\Gamma_z)/(2\pi)$. Note that $V(z)$ must be a periodic function in order to maintain the periodicity of the domain. However, since we have assumed that vertical velocity decreases linearly with height in the system, the initial Gaussian profile had to be contained within the linear part of the sine function as shown in Figure (9a). Therefore, the height of the domain had to be chosen large enough. The vertical extent of the domain was on the order of $1000d$, and had to be increased with higher C_0 since f_{crit} increases with C_0. To reduce the computational cost, some of the later simulations at very high C_0 were performed with a high-order polynomial function for settling velocity of the form $V = -sz(m^{20} - z^{20})/(m^{20})$, where $m = \Gamma_z/2$. This formulations allowed the vertical extent of the domain to be smaller, since the linear part of this function encompasses a greater fraction of the domain than that of the sine function. Figure (9) shows the comparison of the proportion of the linear part of two functions with respect to an initial concentration profile. The polynomial formulation can reduce the required height of the domain by a half.

5.2 Low input mass regime

This section compares the theoretical predictions of the concentration profile to the 3D numerical simulations. From the analytical analysis, it is predicted that a system with $C_0 < C_{crit}$ will converge to a laminar steady state solution given by Equation (18). However,

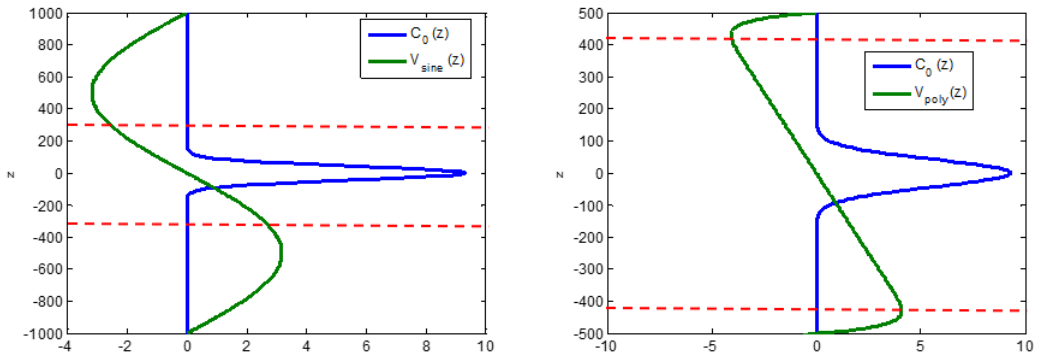

Figure 9: Initial condition $C_{init}(z)$ and two expressions for settling velocity: sinusoidal (left) and polynomial (right). The red dashed lines indicate the region where the settling velocity functions are linear. The polynomial function is linear for a greater fraction of the domain than the sinusoidal function.

for a system with an input mass $C_{crit} < C_0 < C_{conv}$, then the system is predicted to develop double diffusive instabilities, and a steady state profile can be, in theory, approximated by the piecewise profile from Equations (53) - (55). In this study, we fixed $\tau = \text{Pr} = 0.1$ and varied f_∞ from 10 to 100 (corresponding to settling velocity gradients $s = 0.01$ and 0.001 respectively). We examined systems with $C_0 = 0.5C_{crit}$ and $C_0 = 2C_{crit}$ to determine whether the double diffusive instabilities occured. For the system with $f_\infty = 10$, we find that $C_{crit} = 4$ and for $f_\infty = 100$, $C_{crit} = 46$. Figure (10) shows horizontally-averaged concentration profiles $C_{init}(z)$ at steady state, with $f_\infty = 10$ in the upper panel and $f_\infty = 100$ in the lower panel. The systems with $C_0 = 0.5C_{crit}$ are on the left side, and the systems with $C_0 = 2C_{crit}$ are on the right side. Each plot shows the theoretical prediction for the steady state profile from piecewise theory in blue, using a laminar Gaussian solution in green, and finally, the actual 3D horizonatally-averaged concentration profile in red dots. When $C_0 < C_{crit}$, the theory predicts that the system should be stable. The results from 3D simulations and the theoretical prediction overlay the laminar Gaussian steady state solution, showing that the system is indeed stable. When $C_0 > C_{crit}$, the theory predicts that double diffusive instabilities will develop. The 3D simulation results deviate from the laminar Gaussian steady state solution due to the effects of double diffusive instabilities in the region where $z < 0$. Furthermore, the steady state concentration profiles calculated from (53)-(55) fit the 3D simulation results extremely well. This shows that our estimates of the steady state profile of low-mass iron-rich layers are good predictors of the actual results.

5.3 Higher input mass regime

We have also investigated whether the theoretical approximations are valid for systems with higher input C_0. For $\tau = \text{Pr} = 0.1$ and $f_\infty = 10, 100$, we ran simulations for $C_0 = 100C_{crit}$. To verify that the theory is valid for different values of τ, we also ran a simulation with $\tau = 1/30$, $\text{Pr} = 0.1$, $f_\infty = 10$, $s = 1/300$. Figure (11) shows the concentration profiles $C(z)$ for $\tau = 0.1$, $f_\infty = 10$ on the left and $f_\infty = 100$ on the right, and the simulation with $\tau = 1/30$

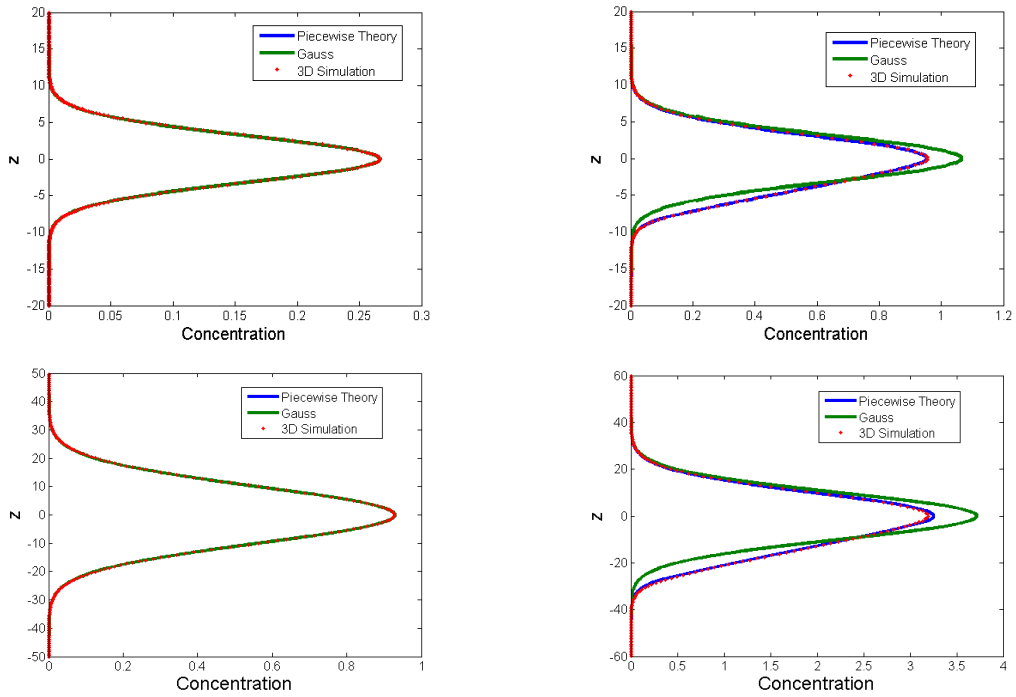

Figure 10: Steady state concentration profiles as a function of z-direction for systems with low input mass. The figures in the upper panels are from simulations with $f_\infty = 10$, and the figures in the lower panels with $f_\infty = 100$. The figures on the left side are from simulations with input mass below C_{crit}, such that $C_0 = 0.5C_{crit}$, and the figures input mass above C_{crit}, such that $C_0 = 2C_{crit}$. The blue line indicates concentration profile from piecewise analytical theory, green line is Gaussian laminar solution, and red dots show horizontally-averaged concentration from 3D simulations.

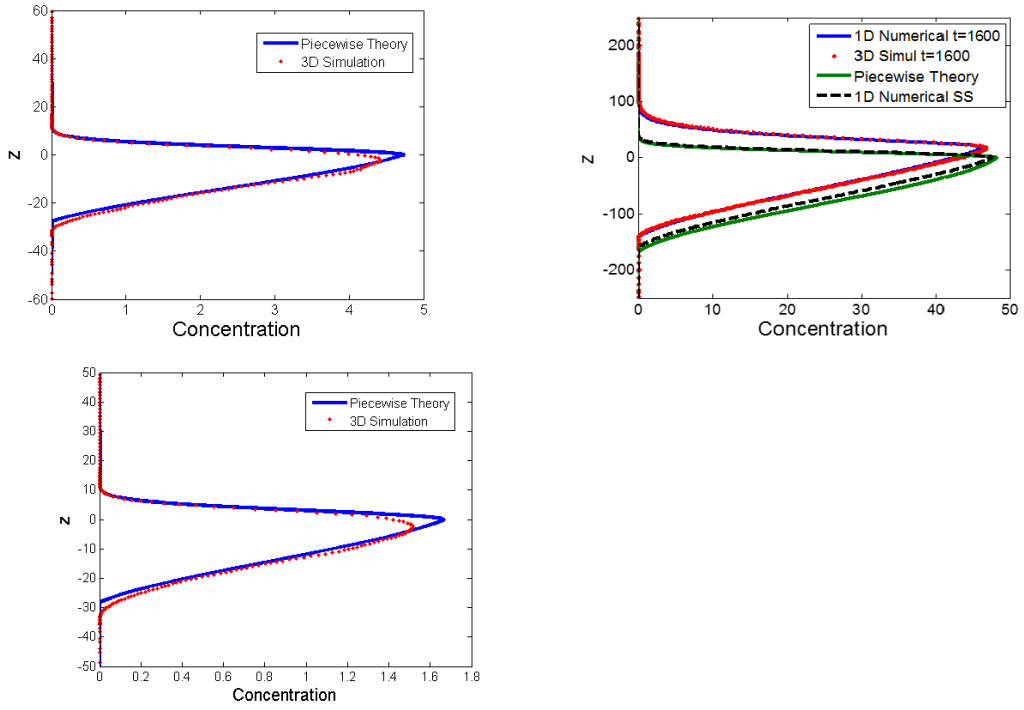

Figure 11: Concentration profiles as a function of z-direction for systems with higher input $C_0 = 100C_{crit}$. The figure on the left is from simulations with $f_\infty = 10$, $\tau = 0.1$, the figure on the right has $f_\infty = 100$, $\tau = 0.1$, and the figure on the bottom has $f_\infty = 10$, $\tau = 1/30$.

on the bottom. In the first two cases, the 3D simulation results and theoretical piecewise concentration profile agree very well. The last 3D simulation took a long time, and we were unable to reach a steady state in a given time frame. Therefore, for the $f_\infty = 100$ simulation, a 1D simulation based on Equation (39) with the same input parameters was run to steady state, and the results from the 1D simulation were compared with the results from the 3D simulations as well as the theoretical piecewise steady state concentration profile. The figure shows an agreement between 1D simulation and 3D horizontally-averaged simulation results at the same time $t = 1600$, and an agreement between the steady state concentration profiles from 1D simulation and the piecewise analytical formula. Therefore, the transient solutions of the 3D problem can be well-approximated by solving Equation (39), and the steady state concentration profiles are given by analytical piecewise approximation (53)-(55) even for systems with higher input mass.

5.4 Fully-convective regime

Finally, we tested the theoretical prediction for the input mass criteria for the transition from double diffusively unstable to the fully convective regime. Because the simulations with high input mass and large f_∞ values are computationally expensive, we ran simulations with $f_\infty = 10$, $\tau = \mathrm{Pr} = 0.1$, $s = 0.01$. For these input parameters, $C_{conv} = 4400$, so we ran simulations with greater input mass, $C_0 = 4500$, for which the system is predicted to be fully

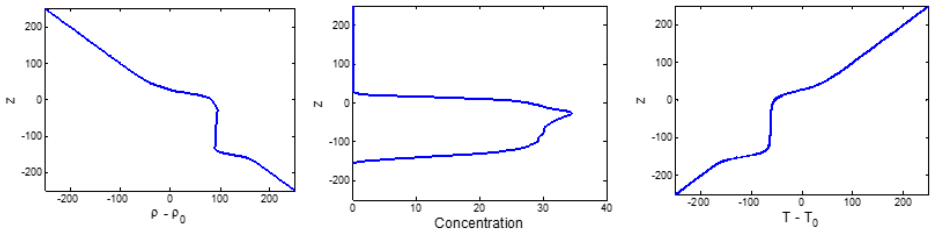

Figure 12: Vertical profiles of density deviations from background density, compositional concentration, and temperature deviations from background temperature for a fully convective simulation with input parameters: $f_\infty = 10$, $\tau = \mathrm{Pr} = 0.1$, $s = 0.01$, $C_0 = 4500$. The density and temperature profiles appear fully mixed within the convective layer.

convective, and with lower input mass, $C_0 = 4000$ and $C_0 = 3500$, which are predicted to be only double diffusively convective. However, the results from the 3D simulations showed that all three systems were fully convective, making the prediction for C_{conv} inaccurate. Such results may be due to the limitation of the validity of assumptions in the theory for the prediction of a steady state profile, as described in Section 4. A better estimate for C_{conv} needs to be derived in the future.

Figure (12) shows the vertical profiles of the density deviations away from background density ρ_0, from the compositional concentration, and the temperature deviations away from the background temperature T_0, from the simulation with $C_0 = 4500$. Both density and temperature profiles appear to be well-mixed in the fully convective region, while the concentration profile is not as well mixed by convection. As a system becomes closer to being fully convective, the background temperature gradient is no longer maintained constant, violating one of the assumptions of the piecewise theory. What determines the thickness of the fully convective layer as a function of C_0, τ, Pr, and s remains to be determined. In addition, we observed gravity waves generated in 3D simulations with high input mass, which could also alter the transport in and out of the "pinched" layer. The generation of the waves can be observed from the horizontal velocity field, as shown in Figure (13).

6 Discussion

In this work, we modelled the distribution of iron in the outer layer of a star, assuming that it settles from the top and is levitated from the bottom. We found that the laminar steady state solution, in absence of convective instabilities in the system, approaches a Gaussian distribution, which is dependent on 3 parameters: the total amount of iron, the ratio of thermal diffusivity to particle diffusivity, and the slope of the settling velocity profile.

We also studied the iron concentration profiles in systems which become double diffusively unstable. In particular, we found an analytical prediction for total mass of iron in the system, for a given Prandtl number, diffusivity ratio, and settling velocity slope, above which the system becomes double diffusively unstable rather than approach the laminar steady state solution. We also developed a semi-analytical piecewise concentration profile that approximates the steady state solution for systems that are double diffusively unsta-

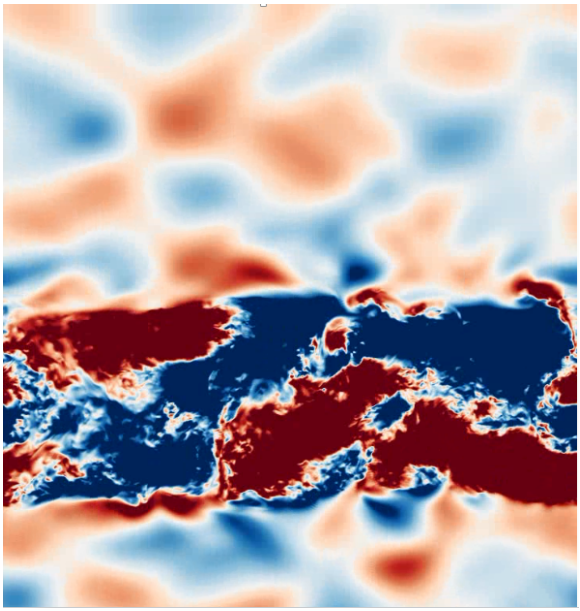

Figure 13: Horizontal velocity field for xz-plane from a fully convective 3D simulation. Positive velocity is in warm colors, negative in cool colors. The 45-degree alternative pattern of velocity field indicates gravity waves travelling toward the "pinched layer" (super-saturated region).

ble. Our theoretical predictions agreed well with the vertical concentration profiles from 3D simulation runs for several values of input masses, Prandl numbers, diffusivity ratios and settling velocity slopes. In addition, we found that the transient concentration profiles obtained from a 1D code that solves (39) agree with the vertical concentration profiles from 3D simulations at the same time steps. These conclusions are important for the development of the stellar evolution models, especially if iron layers do play a role in the pulsations of certain stars. These models are complex, and the incorporation of a 1D approximation or a piecewise theoretical solution into the model is more suitable than running a full 3D simulation for the double diffusive process.

Since this work developed tools to approximate steady state and transient solutions for systems that are either stable or double-diffusively unstable, the next step is to develop a theoretical model for the concentration profiles in a fully convective system. However, as the system becomes fully convective, the underlying assumption of constant background temperature gradient is violated. In addition, as the fluid is continuously mixed in such system, defining a steady state or reaching a steady state through simulations may be difficult. In the 3D simulations with full convection, we observed gravity waves that transport material into and out of convective layer. The influence of these waves most likely also needs to be taken into consideration when developing a model for a fully convective layer.

7 Acknowledgements

I would like to thank my advisor, Pascale Garaud, for her invaluable guidance and continuous supervision throughout the summer and help with revising this report. I am also thankful to the directors for organizing a smooth program, and to all of the faculty members and summer participants for insightful discussions and a memorable summer.

References

[1] P.G. Baines and A.E. Gill, *On thermohaline convection with linear gradients*, J. of Fluid Mechanics, 37 (1969), pp. 289–306.

[2] J.M. Brown, P. Garaud, and S. Stellmach, *Chemical transport and spontaneous layer formation in fingering convection in astrophysics*, Astrophysical Journal, 768 (2013), pp. 34–95.

[3] J. P. Cox, *On second helium ionization as a cause of pulsation instability in stars*, Astrophysical Journal, 138 (1963), pp. 487–536.

[4] M. Kiriakidis, M.F. El Eid, and W.Glatzel, *Heavy element opacities and the pulsations of beta cepheid stars*, Monthly Notices of the Royal Astronomical Society, 255 (1991), pp. 1–5.

[5] E.A. Spiegel and G. Veronis, *On the boussinesq approximation for a compressible fluid*, Astrophysical Journal, 131 (1960), pp. 442–447.

[6] A. Traxler, S. Stellmach, P. Garaud, T. Radko, and N. Brummell, *Dynamics of fingering convection i: Small-scale fluxes and large-scale instabilities*, J. of Fluid Mechanics, 677 (2011), pp. 530–553.

[7] S. Turcotte, J. Richer, and G. Michaud, *Consistent evolution of f. stars: Diffusion, radiative accelerations, and abundance anomalies*, Astrophysical Journal, 504 (1998), pp. 559–572.

[8] S. Vauclair and G. Vauclair, *Element segregation in stellar outer layers*, Ann. Rev. Astronomy and Astrophysics, 20 (1982), pp. 37–60.

[9] S.A. Zhevakin, Russ. Astrophysical Journal, 30 (1953), pp. 161–170.